Journal of Ultrafine Grained and Nanostructured Materials
https://jufgnsm.ut.ac.ir
Vol. 52, No.2, December 2019, pp. 133-141
Print ISSN: 2423-6845 Online ISSN: 2423-6837
DOI: 10.22059/jufgnsm.2019.02.01

Photocatalytic degradation of methylene blue by 2 wt.% Fe doped TiO_2 nanopowder under visible light irradiation

Nikta S. Moalej, Sina Ahadi, Saeed Sheibani*

School of Metallurgy and Materials Engineering, College of Engineering, University of Tehran, Tehran, Iran.

Recieved: 9 October 2019; Accepted: 29 November 2019
** Corresponding author email: ssheibani@ut.ac.ir*

ABSTRACT

In this paper, 2wt.% Fe doped TiO_2 nanopowder was prepared by a combination of sol-gel and mechanical alloying methods. The mechanical alloying of Fe powder with $Ti(OH)_4$ gel produced from the sol-gel method was used to produce Fe doped TiO_2 nanopowder. The synthesized samples were characterized by X-ray diffraction (XRD), field emission scanning electron microscopy (FESEM) and diffuse reflectance spectroscopy (DRS). The photocatalytic behavior of nanopowder was examined by the degradation of methylene blue (MB) under visible light irradiation. XRD result showed that the phase structure was a combination of anatase and rutile phases and the anatase percentage was considerably increased to 72.3 % by Fe doping. The FESEM results demonstrated that the average particle size of TiO_2 was decreased to 45 nm by Fe doping through ball milling. DRS results indicated the band gap of photocatalyst has shifted from 2.95 to 2.60 eV by Fe doping through ball milling. Photodegradation of MB was evaluated and the degradation rate was reached to 47% after 240 min under visible light irradiation. The photocatalytic performance of TiO_2 nanoparticles improved by doping Fe through mechanical milling. Degradation reaction conformed by the first-order reaction kinetic model. The recycled Fe doped TiO_2 nano-photocatalyst showed only a slight decrease of 7% in degradation rate after the third cycle.

Keywords: *TiO_2; Nano-photocatalyst; Doping; Sol-Gel; Mechanical Milling.*

1. Introduction

Dyes and pigment are materials that are commonly used in the textile and other printing industries. These dyes are harmful to the environment and cause serious water pollutions. These organic contaminants affect wastewaters thus dyeing industries are considered as the high pollution ones [1]. MB is a cationic dye, used extensively for dyeing cotton. This is used as an example of textile dyes [2]. In the textile industry, only part of dyes is utilized, the rest of this dyestuff dissolves in wastewater and affects water sources such as rivers and lakes. To decrease dye pollution, different methods such as adsorption, electro and chemical coagulation, ultrasonic decomposition, advanced chemical oxidation and nanofiltration were used to remove dyes from wastewater [3]. Photocatalytic degradation has been a promising method for eliminating dyes and different pigments from the wastewater of the textile industry [4]. Recently, using semiconductor materials as the photocatalyst is a rising technology [5]. Semiconductors under the illumination of photons with energy, more than their band gap, produce electron-hole pairs which result in oxidation of a large category of organic compounds. There are

several different semiconductors like ZnO, Fe_2O_3, and WO_3 which have photocatalytic properties, but TiO_2 has shown great superiority compared with the other materials so far. The reasons for this choice are nontoxicity, low cost and availability [6]. This semiconductor has unique structural and electronic properties. TiO_2 has three structures of anatase, rutile and brookite. Anatase and rutile have a high band gap energy of 3.23 and 3.00 eV, respectively [7]. Many factors affect the photocatalytic behavior of TiO_2 like crystal structure and morphology. For example, photocatalytic activity was increased by the decrease of particle size to nanoscale [8]. Another way to improve the photocatalytic activity is doping of TiO_2 by different elements. It is possible to decrease the band gap of TiO_2 into the visible light range [9]. Different metals such as Cu, Fe, Ag and Au were used as the dopants for TiO_2 to improve its photocatalytic activity. Among these doped TiO_2 photocatalysts, Fe doped TiO_2 has received considerable attention because of increased photocatalytic efficiency in many cases. There are various methods used to dope these elements in TiO_2, such as chemical and solid-state methods [10-14]. Nevertheless, most of the current methods face some issues like low production yield and the use of some toxic chemical compounds. Therefore, the development of a new fabrication method is still required. High energy mechanical milling is a solid-state method used to dope Fe in TiO_2. The advantages of this method are the production of powder in the nanometer scale, simplicity and low cost. It should be emphasized that the production of nano-photocatalyst by mechanical milling and therefore the increase in the surface area has a significant effect on improving the photocatalytic performance of the product. Sanchez et al. [15] prepared Fe doped TiO_2 by mechanical alloying of TiO_2 and Fe as the chemical precursors. Also, Fe doped TiO_2 powder was prepared using mechanical milling of TiO_2 and iron oxide powder [16]. Eadi et al [17] developed Fe doped TiO_2 nanopowder using mechano-chemical milling of $FeCl_3$ and TiO_2 powder. However, there are very few reports of preparing Fe doped TiO_2 nanopowder by the combination of sol-gel and mechanical alloying method. Hence in this work, the mechanical alloying of Fe powder with $Ti(OH)_4$ gel produced from the sol-gel method was studied to produce Fe doped TiO_2 nanopowder. Also, the photocatalytic degradation of MB by produced photocatalyst as well as degradation kinetics was investigated.

2. Experimental procedure

The starting materials were tetrabutyl orthotitanate (TBOT) as a titanium source, ethanol as the solvent, benzyl alcohol (BA) as a surfactant and distilled water as the hydrolysis agent. In the first stage, $Ti(OH)_4$ gel was prepared by the sol-gel method. A solution of distilled water and benzyl alcohol was added to ethanol. Then TBOT was added to ethanol dropwise. The total molar ratio of TBOT: H_2O: Ethanol: Benzyl alcohol was in respect 1:5:100:5. In the room temperature, the final solution was stirred for 1 h with magnetic stirring. The solution was centrifuged with a speed of 3000 rpm and the $Ti(OH)_4$ gel was dried in an oven at 80 °C for 24 h. In the second stage, for doping of Fe (2 wt.%) and prepared gel powder mixture was mechanically milled for 3, 5 and 7 h with a planetary ball mill (PM2400 model) and 5 h of ball milling was selected for further investigation. The ball to powder weight ratio and milling speed were 25 and 250 rpm, respectively. In the third stage, the mechanically milled powders were heat treated at 500 °C for 2 h. For comparison, undoped TiO_2 samples were also synthesized; pure TiO_2 sample without ball milling (denoted as TiO_2 sample) and 5 h ball milled pure TiO_2 sample (denoted as $BMTiO_2$). Besides, the Fe doped sample was denoted as the Fe-$BMTiO_2$ sample. According to a previous study [18] that iron content between 1 and 10 wt.% was doped in TiO2 by the sol-gel method. The results showed that up to 2 wt.%, the Fe ions are incorporated into the lattice of TiO2, and substitute the Ti ions. With the higher Fe content, only part of Fe ions enters the lattice of TiO2. As a result, this value is selected in this study.

The powder has been characterized by XRD (Philips PW3040/60) with radiation of Cu-K_α and to study the structure, FESEM (CamScan MV2300) to study microstructure, DRS (Shimadzu, MPC-2200) analysis to study the optical properties. The crystallite sizes of the samples were estimated by applying the Scherrer equation [19]. The lattice parameters were determined using the following equations.

$$d_{(hkl)}=\frac{\lambda}{2d\sin\theta} \quad \text{(eq. 1)}$$

$$\frac{1}{d^2_{(hkl)}}=\frac{h^2}{a^2}+\frac{k^2}{b^2}+\frac{l^2}{c^2} \quad \text{(eq. 2)}$$

where, $d_{(hkl)}$ is the distance between crystal planes

of (hkl), λ is the wavelength of X-ray used, θ *i*s the Bragg angle, hkl is the crystal plane indices and a, b, and c are lattice parameters (in a tetragonal phase a = b ≠ c). It should be noted that the instrumental error has been removed by Warren's method [20].

The photocatalytic performance of samples was evaluated based on MB degradation in an aqueous solution under visible light irradiation (Osram, 150 W). 50 mL aqueous solution of MB with a concentration of 5 ppm was placed into the reaction vessel, and photocatalyst powder (0.4 mg/L) was added. Before irradiation, the suspensions were magnetically stirred in the dark for 1 h to establish the adsorption equilibrium. At certain time intervals, 1 mL of solution were removed and centrifuged to remove photocatalyst particles. The solutions were then analyzed using the UV-Vis spectrophotometer (UNICO 2100) for the measurements of the maximum absorbance at 664 nm for MB. Finally, this process was repeated three times to investigate the stability of the photocatalyst. According to the Lambert-Beer law [21], the degradation rate of MB was calculated by the following equation.

$$\frac{C}{C_0} = \frac{A}{A_0} \quad \text{(eq. 3)}$$

where, C_0 and C are the concentration of initial MB and at time t, respectively. Also, A_0 and A are the absorbances of the initial MB aqueous solution and at time t, respectively.

3. Results and Discussion

To obtain an optimal time of ball milling, the powder sample was ball milled for 3, 5 and 7 h. Initial characterization of the morphology of the as-prepared gel powder by SEM in Fig. 1 (a) showed that the average particle size is 60 μm. Also, the particle size decreases after 3 and 5 h of ball milling to the average value of 650 and 220 nm, respectively, as shown in Figs. 1 (b) and (c). However, the average particle size increases to the average value of 900 nm by the progress of milling to 7 h, as shown in Fig. 1 (d). This is possibly due to the adherence and agglomeration of ultrafine particles into larger particles. Accordingly, 5 h of ball milling was selected for further investigation.

To analyze the structure of powders, these synthesized samples before and after calcination

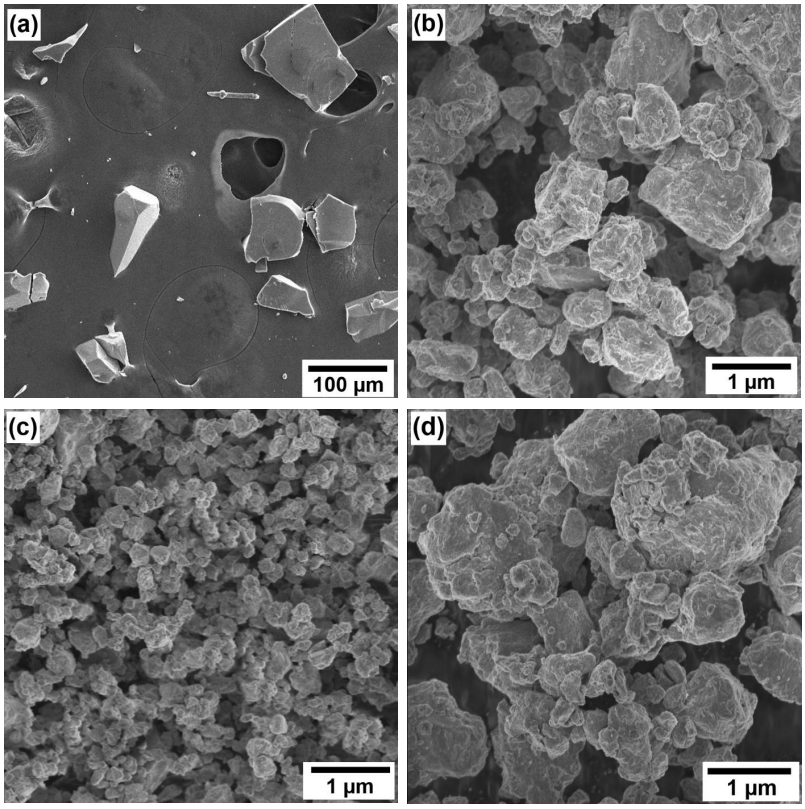

Fig. 1- FESEM images of the as-prepared gel powder after different milling times of (a) 0, (b) 3, (c) 5 and (d) 7 h.

heat treatment were analyzed by XRD. All the XRD patterns of samples in Fig. 2 before calcination do not show any characteristic peaks indicating the amorphous structure of powders. It seems that the structure was not changed by ball milling and Fe addition. However, after calcination, the crystalline structures were formed and the characteristic peaks of both anatase and rutile phases could be identified by JCPDS file no. 21-1272 and no. 21-1276, respectively. There are no significant differences between the XRD patterns of different samples. The characteristic peak of Fe is not detectable in the XRD pattern possibly due to its good dispersion in the TiO_2 structure. Another reason for this is the Fe doping in the TiO_2 structure. To study the structure in detail, the fraction of the anatase phase can be estimated from the intensities of XRD peaks using the following equation [22].

$$\text{Fraction of Anatase (\%)} = \frac{100}{(1+1.26(I_R/I_A))} \quad \text{(eq. 4)}$$

where, I_R and I_A correspond to the intensity of the XRD most intense peaks of rutile and anatase, respectively. The results of lattice parameters and the fraction of the anatase phase in different samples are presented in Table 1. As summarized in this Table, for the undoped TiO_2 nanopowder and ball milled sample the fraction of anatase phase was relatively similar; about 53 %. Also, the anatase percentage was considerably increased to 72.3 % by Fe doping. This indicates that, when comparing with the Fe doping effect, ball

Table 1- Influence of ball milling and Fe doping on the fraction, lattice parameters and crystallite size of anatase phase.

Sample	Fraction of anatase (%)	Lattice parameters (Å)		Crystallite size (nm)
		a=b	c	
TiO_2	52.3 ± 3.14	3.7861 ± 0.1135	9.6360 ± 0.2890	61 ± 3
$BMTiO_2$	53.4 ± 3.2	3.7860 ± 0.1135	9.6358 ± 0.2890	39 ± 2
Fe-$BMTiO_2$	72.3 ± 4.3	3.7862 ± 0.1135	9.7112 ± 0.2890	23 ± 2

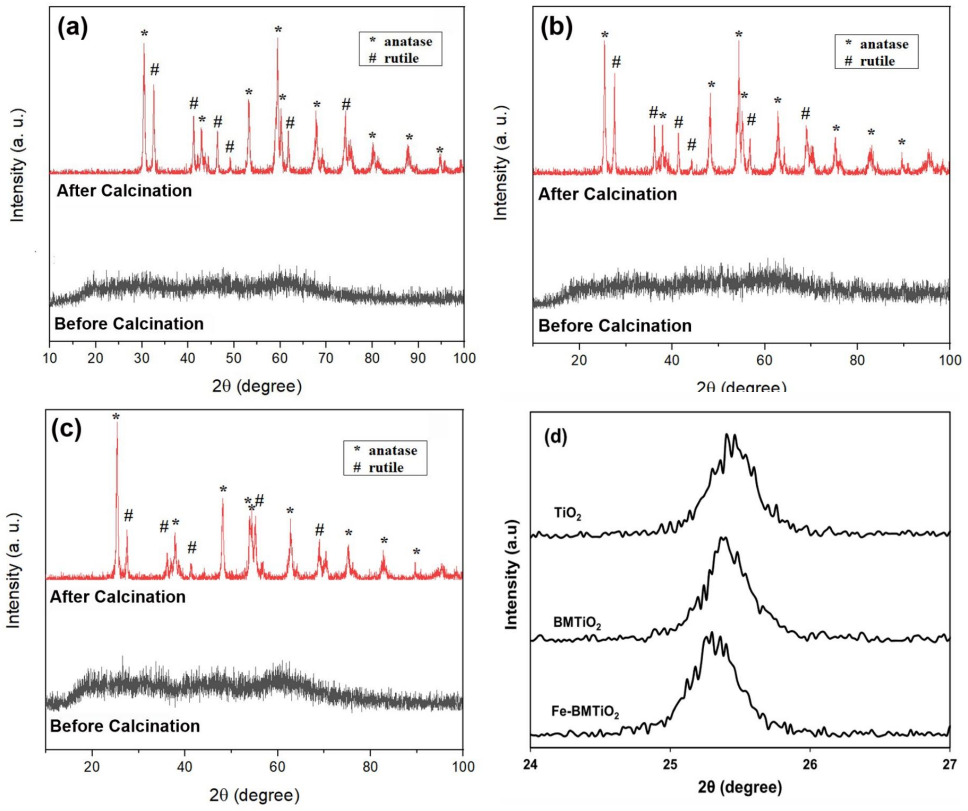

Fig. 2- XRD patterns of (a) TiO_2, (b) $BMTiO_2$ and (c) Fe-$BMTiO_2$ samples before and after calcination and (d) is the comparison of an enlarged view of peaks at 2θ range of 24 to 27°.

milling has no significant influence in anatase-to-rutile transformation. On the other hand, the supersaturated solid solution resulted from Fe doping [23, 24] can delay and inhibit the formation of the rutile phase. Furthermore, the XRD peaks of the crystal plane (101), (200) and (004) of anatase were selected to determine the lattice parameters. The calculated lattice parameters of all samples are shown in Table 1. The a and c values estimated for TiO_2 and $BMTiO_2$ samples were not varied much with the ball milling, whereas those estimated for Fe doped TiO_2 (Fe-$BMTiO_2$ sample) were increased. This increase was considerably higher for c lattice constant. As shown in Fig. 2 (d), it can be found that the peaks of Fe doped TiO_2 sample (Fe-$BMTiO_2$ sample) were shifted towards a lower angle compared to that of other samples. This shows the increase of interplanar spacing with Fe doping which agrees well with previous work [25]. The reason is the structural distortions due to the replacing of Ti ions with Fe ions. This could be expected from a different atomic radius of Fe ions (0.785 Å) and Ti ions (0.745 Å) [26]. The crystallite sizes for the TiO_2, $BMTiO_2$ and Fe-$BMTiO_2$ samples were found to be 61, 39 and 23 nm, respectively. The decrease from 61 to 39 nm was related to the lattice defects and thus grain refinement due to the mechanical energy from ball milling [27]. Also, upon doping with 2 wt.% Fe the crystallite size value decreased to 23 nm. This result suggests that the Fe^{3+} doping into the TiO_2 lattice effectively inhibits the anatase grain growth by providing dissimilar boundaries [28, 29].

FESEM images of different samples after calcination are showed in Fig. 3. It can be seen that the morphology of the Fe-$BMTiO_2$ powder is completely different from those of TiO_2 and $BMTiO_2$ powders. Pure TiO_2 powders (Figs. 3 (a) and (b)) consist of a relatively larger and micron size chuck of particles. However, the primary particles with an average size of about 300 nm can be observed in the TiO_2 sample in Fig. 3 (a). Fig. 3 (b) reveals that although the degree of agglomeration increased by mechanical milling in pure TiO_2 powder, the particles are finer (average size of about 180 nm). Whereas, Fe doped TiO_2 sample (Fig. 3 (c)) consists of nano-sized primary particles with a spherical shape. Higher magnification FESEM image in the inset showed that the average size of TiO_2 particles was decreased to about 45 nm by Fe doping through ball milling. Hence, the growth of TiO_2 particles is prevented by Fe doping [30,31], which is conducive to improve the photocatalytic activity of TiO_2 nanopowder.

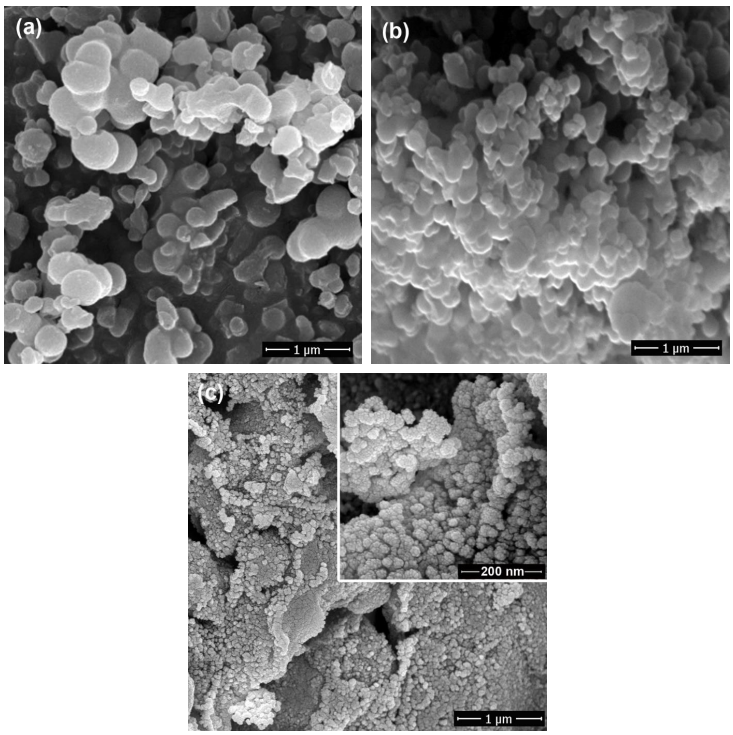

Fig. 3- FESEM images of (a) TiO_2, (b) $BMTiO_2$ and (c) Fe-$BMTiO_2$ samples after calcination.

To study the optical absorption properties of photocatalysts, DRS of powders was examined and the band gap energy values were calculated using the Tauc plot [32]. Band gap energies were estimated by extrapolation $(\alpha \times h\nu)^{1/n}$ versus the energy curve with a linear behavior. The value of n assumed to be 2 due to the previous researches suggesting TiO_2 nanoparticle has an indirect transition band gap [33].

$$(\alpha h\nu)^{1/n} = A(h\nu - E_g) \quad \text{(eq. 5)}$$

where, hν is the photon energy, E_g is the band gap, A is a constant, and α is the absorption coefficient. DRS spectra and Tauc plots of different samples after calcination are presented in Fig. 4. Pure TiO_2 powder did not show any absorption within the visible light region whereas the Fe doped TiO_2 nanopowder significantly showed a red shift towards longer wavelengths. The decrease in the band gap energy of TiO_2 from 2.95 (TiO_2 sample) to 2.60 eV (Fe-$BMTiO_2$ sample) is related to the interaction of the 3d orbital of Ti and d orbital of Fe introducing intra-band gap states that result in the red shift in the absorption of light [34,35]. However, compared with Fe-$BMTiO_2$ nanopowder, the band gap of the $BMTiO_2$ sample had a slight shift towards visible light, 2.72 eV. Smaller band gap energy of the $BMTiO_2$ sample in comparison with the TiO_2 sample is possibly related to the smaller crystallite and particle sizes ascribed to ball milling, as confirmed by the above results. It has been reported that the band gap of semiconductor crystalline is a function of the particle size [23,36,37]. The density of point/surface defects of semiconductor crystalline has been changed with a decrease in particle size. Due to mild delocalization of molecular orbitals on the surface, defects in the bulk semiconductor create deep and shallow traps near the band edge of its electronic state, which brings about a reduction in band gap, that is, red shift in the absorption spectrum. This indicated that the band gap of TiO_2 nano-photocatalyst was narrowed by Fe doping through ball milling and light with lower energy could be used to excite the photocatalysis. Fe-BMTiO2 sample shows much higher visible light absorption than other samples in the whole visible light region, which suggests that Fe additive promotes visible light absorption in TiO_2. The enhanced visible light absorption is attributed to the surface plasma resonance effect from Fe under visible light illumination [38].

The photocatalytic efficiency of prepared photocatalysts was evaluated by degradation of 5 ppm MB solution under visible light irradiation. Figs. 5 (a), (b) and (c) show the UV-Vis spectra of the MB solution with the different time intervals. A maximum absorption band of MB solution can be seen at 664 nm. The higher photocatalytic efficiency of Fe doped TiO_2 nanopowder in MB degradation was observed from the gradual decrease of absorption peak intensity (Fig. 5 (c)). However, the peak intensity was not changed considerably with irradiation time in the presence of pure TiO_2 photocatalysts (Figs. 5 (a) and (b)). This is due to the pure TiO_2 samples cannot absorb the visible light. Fig. 5 (d) shows the plot of C/C_0 versus time for the degradation of MB using different photocatalysts under visible light irradiation. It can be seen that only 3% of the MB was degraded after 240 min in

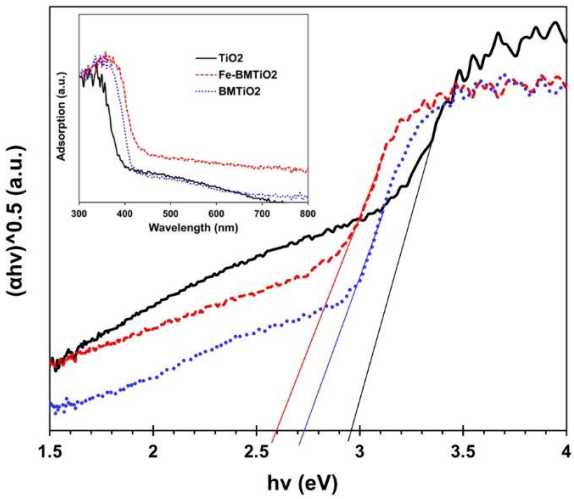

Fig. 4- Tauc plots and UV-vis diffuse reflectance spectra of different samples after calcination.

the presence of pure TiO_2. Lower activity of TiO_2 ascribed to the inefficient absorbance of photons under visible light due to its large band gap. Also, the MB degradation rate by $BMTiO_2$ photocatalyst was increased to 7%. Significant enhancement in the degradation rate to 47% was observed with Fe doped photocatalyst.

The first-order reaction kinetics model (Eq. 6) was used to fit the data obtained from the MB degradation using Fe doped TiO_2 nano-photocatalysts under visible light irradiation.

$$-\ln(C/C_0) = kt \qquad \text{(eq. 6)}$$

where, t is the time and k is the reaction rate constant [39]. The fitting curve is presented in Fig. 6. A good linear relationship with R^2= 0.9687 indicates the photocatalytic degradation process of MB conforms to the first-order reaction kinetics. The slope represents the reaction rate constant k of 0.0027 min^{-1}. The enhanced degradation efficiency of MB occurred by Fe doped nano-photocatalyst was mainly due to the lower band gap energy of this sample. It should be noted that smaller particle size and hence higher surface area was possibly another reason for faster degradation rate. Besides, the presence of both anatase and rutile phases was beneficial to higher photocatalytic activity. The results of MB degradation using the recycled Fe doped TiO_2 nano-photocatalyst showed only a slight decrease of about 7% in degradation rate after the third cycle. This indicates the excellent recyclability of prepared nano-photocatalyst. The slight decrease may be related to the little loss of the photocatalyst and small inactivation of the photocatalyst by remnant MB or the reaction products [40].

4. Conclusion

In this study, 2 wt.%Fe doped TiO_2 nanopowder was prepared by 5 h ball milling of Fe and $Ti(OH)_4$ gel produced by the sol-gel method. Samples were characterized by using XRD, FESEM and DRS techniques. XRD results revealed the presence of both anatase and rutile phases for all the samples. By Fe doping in TiO_2, the anatase percentage was

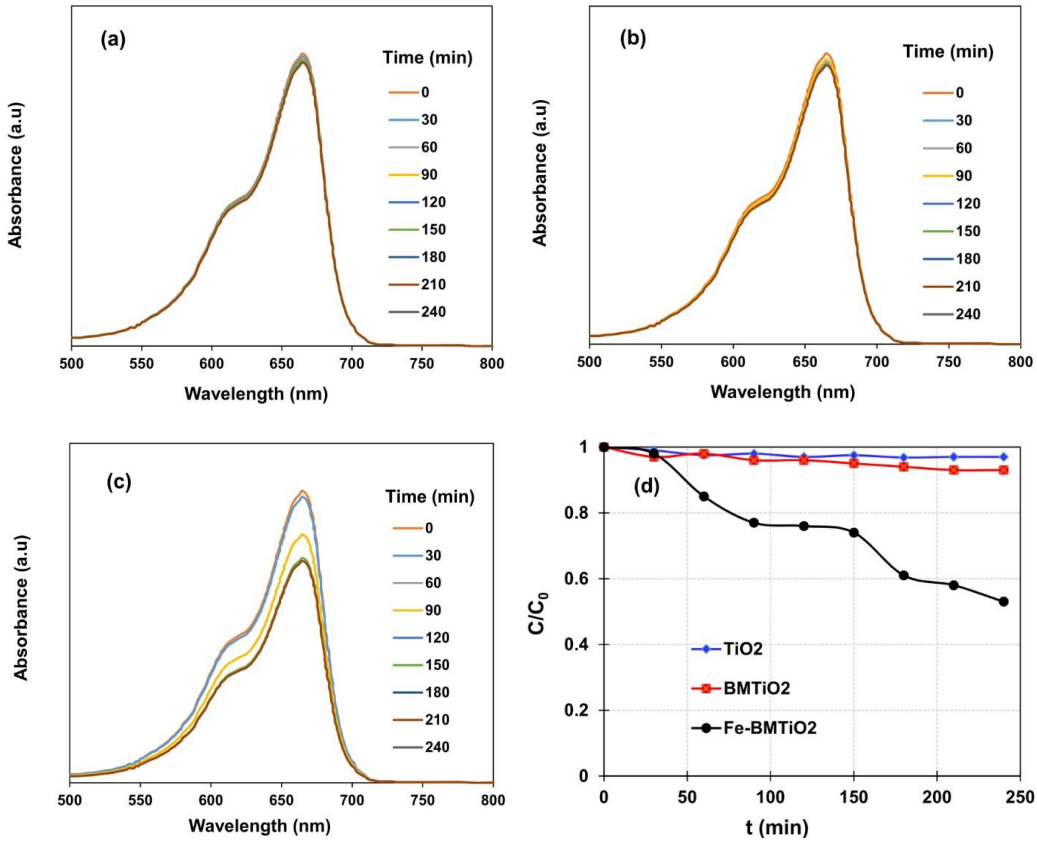

Fig. 5- UV-Vis spectra of 5 ppm MB solution irradiated with visible light over (a) TiO_2, (b) $MBTiO_2$ and (c) Fe-$MBTiO_2$ samples, (d) the MB degradation rate of different within 240 min over different samples.

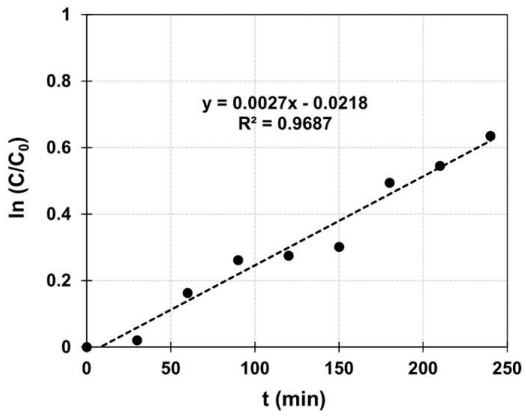

Fig. 6- The plot of $\ln(C/C_0)$ versus time for degradation of 5 ppm MB solution using Fe doped TiO_2 nanopowder under visible light irradiation. The dashed line shows the corresponding linear fitting curves using the first-order reaction kinetic model.

considerably increased to 72.3 % and the estimated lattice parameter of c was decreased. The average size of the Fe doped TiO_2 particle was 45 nm. It can be seen that by Fe doping in TiO_2, the band gap energy was decreased to 2.60 eV, which is consistent with the red shift of absorption edge observed in DRS spectra. Also, the effect of Fe doping on the photodegradation of MB under visible light was investigated. Fe doping in TiO_2 improved its capability of photocatalytic degradation of MB solution (47%) after 240 min under visible light. However, only 3% of MB was degraded in the presence of pure TiO_2 photocatalyst. The kinetics of MB photodegradation was investigated in detail. The photocatalytic performance and fabrication convenience enabled by the novel method presented in this research opens a new route to the applications of TiO_2 under visible light.

5. Acknowledgments

The authors would like to acknowledge the support of the University of Tehran for this research. Also, the financial supports of the Iran Nanotechnology Initiative Council are gratefully acknowledged.

References

1. Lee B-N, Liaw W-D, Lou J-C. Photocatalytic Decolorization of Methylene Blue in Aqueous TiO2 Suspension. Environmental Engineering Science. 1999;16(3):165-75.
2. Salehi M, Hashemipour H, Mirzaee M. Experimental Study of Influencing Factors and Kinetics in Catalytic Removal of Methylene Blue with TiO2 Nanopowder. American Journal of Environmental Engineering. 2012;2(1):1-7.
3. Wu C-H, Chern J-M. Kinetics of Photocatalytic Decomposition of Methylene Blue. Industrial & Engineering Chemistry Research. 2006;45(19):6450-7.
4. Tae Kwon Y, Yong Song K, In Lee W, Jin Choi G, Rag Do Y. Photocatalytic Behavior of WO3-Loaded TiO2 in an Oxidation Reaction. Journal of Catalysis. 2000;191(1):192-9.
5. Tang WZ, Huren A. UV/TiO2 photocatalytic oxidation of commercial dyes in aqueous solutions. Chemosphere. 1995;31(9):4157-70.
6. Nagaveni K, Sivalingam G, Hegde MS, Madras G. Photocatalytic Degradation of Organic Compounds over Combustion-Synthesized Nano-TiO2. Environmental Science & Technology. 2004;38(5):1600-4.
7. Nasralla N, Yeganeh M, Astuti Y, Piticharoenphun S, Shahtahmasebi N, Kompany A, et al. Structural and spectroscopic study of Fe-doped TiO2 nanoparticles prepared by sol–gel method. Scientia Iranica. 2013;20(3):1018-22.
8. Jang HD, Kim S-K, Kim S-J. Effect of particle size and phase composition of titanium dioxide nanoparticles on the photocatalytic properties. Journal of Nanoparticle Research. 2001;3(2-3):141-7.
9. Abazović ND, Mirenghi L, Janković IA, Bibić N, Šojić DV, Abramović BF, et al. Synthesis and Characterization of Rutile TiO2 Nanopowders Doped with Iron Ions. Nanoscale Research Letters. 2009;4(6):518-25.
10. Park HS, Kim DH, Kim SJ, Lee KS. The photocatalytic activity of 2.5wt% Cu-doped TiO2 nano powders synthesized by mechanical alloying. Journal of Alloys and Compounds. 2006;415(1-2):51-5.
11. Lei XF, Xue XX, Yang H. Preparation and characterization of Ag-doped TiO2 nanomaterials and their photocatalytic reduction of Cr(VI) under visible light. Applied Surface Science. 2014;321:396-403.
12. Selvam K, Swaminathan M. Au-doped TiO2 nanoparticles for selective photocatalytic synthesis of quinaldines from anilines in ethanol. Tetrahedron Letters. 2010;51(37):4911-4.
13. Marami MB, Farahmandjou M, Khoshnevisan B. Sol–Gel Synthesis of Fe-Doped TiO2 Nanocrystals. Journal of Electronic Materials. 2018;47(7):3741-8.
14. Al-Jawad SMH, Taha AA, Salim MM. Synthesis and characterization of pure and Fe doped TiO2 thin films for antimicrobial activity. Optik. 2017;142:42-53.
15. Sánchez LC, Calle AM, Arboleda JD, Beltran JJ, Barrero CA, Osorio J, et al. Fe-doped TiO2 prepared by mechanical alloying. ICAME 2007: Springer Berlin Heidelberg; 2008. p. 289-94.
16. Effendi M. Effect of doping Fe on TiO2 thin films prepared by spin coating method. 2012.
17. Eadi SB, Kim S, Jeong SW, Jeon HW. Novel Preparation of Fe Doped TiO2 Nanoparticles and Their Application for Gas Sensor and Photocatalytic Degradation. Advances in Materials Science and Engineering. 2017;2017:1-6.
18. Zhu S, Liu W, Wei S, Fan C, Li Y. Local Structure around Iron Ions in Anatase TiO2. AIP Conference Proceedings: AIP; 2007.
19. Jenkins R, Snyder RL. Introduction to X-ray Powder Diffractometry. John Wiley & Sons, Inc.; 1996.
20. Lipson H, Steeple H. Interpretation of X-ray powder diffraction patterns: Macmillan; 1970.
21. Ingle JD, Crouch SR. Signal-to-noise ratio considerations. Spectrochemical Analysis Prentice Hall, Englewood Cliffs, NJ. 1988:135-63.
22. Spurr RA, Myers H. Quantitative Analysis of Anatase-Rutile Mixtures with an X-Ray Diffractometer. Analytical Chemistry. 1957;29(5):760-2.
23. Rino J-P, Studart N. Structural correlations in titanium dioxide. Physical Review B. 1999;59(10):6643-9.
24. Liqiang J, Xiaojun S, Baifu X, Baiqi W, Weimin C, Honggang

F. The preparation and characterization of La doped TiO2 nanoparticles and their photocatalytic activity. Journal of Solid State Chemistry. 2004;177(10):3375-82.
25. Ali T, Tripathi P, Azam A, Raza W, Ahmed AS, Ahmed A, et al. Photocatalytic performance of Fe-doped TiO2nanoparticles under visible-light irradiation. Materials Research Express. 2017;4(1):015022.
26. Choi J, Park H, Hoffmann MR. Effects of Single Metal-Ion Doping on the Visible-Light Photoreactivity of TiO2. The Journal of Physical Chemistry C. 2009;114(2):783-92.
27. Ward TS, Chen W, Schoenitz M, Dave RN, Dreizin EL. A study of mechanical alloying processes using reactive milling and discrete element modeling. Acta Materialia. 2005;53(10):2909-18.
28. Carneiro JO, Azevedo S, Fernandes F, Freitas E, Pereira M, Tavares CJ, et al. Synthesis of iron-doped TiO2 nanoparticles by ball-milling process: the influence of process parameters on the structural, optical, magnetic, and photocatalytic properties. Journal of Materials Science. 2014;49(21):7476-88.
29. Gomathi Devi L, Kottam N, Girish Kumar S, Eraiah Rajashekhar K. Preparation, characterization and enhanced photocatalytic activity of Ni2+ doped titania under solar light. Open Chemistry. 2010;8(1).
30. Asiltürk M, Sayılkan F, Arpaç E. Effect of Fe3+ ion doping to TiO2 on the photocatalytic degradation of Malachite Green dye under UV and vis-irradiation. Journal of Photochemistry and Photobiology A: Chemistry. 2009;203(1):64-71.
31. Ali T, Tripathi P, Azam A, Raza W, Ahmed AS, Ahmed A, et al. Photocatalytic performance of Fe-doped TiO2 nanoparticles under visible-light irradiation. Materials Research Express. 2017;4(1):015022.
32. Tauc J, Grigorovici R, Vancu A. Optical Properties and Electronic Structure of Amorphous Germanium. physica status solidi (b). 1966;15(2):627-37.
33. Samsudin EM, Abd Hamid SB. Effect of band gap engineering in anionic-doped TiO 2 photocatalyst. Applied Surface Science. 2017;391:326-36.
34. Rauf MA, Meetani MA, Hisaindee S. An overview on the photocatalytic degradation of azo dyes in the presence of TiO2 doped with selective transition metals. Desalination. 2011;276(1-3):13-27.
35. Kemp TJ, McIntyre RA. Transition metal-doped titanium(IV) dioxide: Characterisation and influence on photodegradation of poly(vinyl chloride). Polymer Degradation and Stability. 2006;91(1):165-94.
36. Brus LE. Electron–electron and electron-hole interactions in small semiconductor crystallites: The size dependence of the lowest excited electronic state. The Journal of Chemical Physics. 1984;80(9):4403-9.
37. Brus L. Electronic wave functions in semiconductor clusters: experiment and theory. The Journal of Physical Chemistry. 1986;90(12):2555-60.
38. Li Q, Liang W, Ku Shang J. Enhanced visible-light absorption from PdO nanoparticles in nitrogen-doped titanium oxide thin films. Applied Physics Letters. 2007;90(6):063109.
39. Mahmoodi NM, Arami M, Limaee NY, Tabrizi NS. Kinetics of heterogeneous photocatalytic degradation of reactive dyes in an immobilized TiO2 photocatalytic reactor. Journal of Colloid and Interface Science. 2006;295(1):159-64.
40. Shafei A, Salarpour ME, Sheibani S. Effect of intermediate ball milling on the synthesis of Cu-doped TiO2 nano-photocatalyst by sol–gel method. Journal of Sol-Gel Science and Technology. 2019;92(1):173-85.